Composites: Part A 175 (2023) 107800

Contents lists available at ScienceDirect

Composites Part A

journal homepage: www.elsevier.com/locate/compositesa

Laser cutting of basalt fibre reinforced polymers by QCW fiber laser: Interaction mechanisms and effect of laser parameters

C. Leone [a,e,*], R. Porcaro [b], G. Campana [c], S. Genna [d,e]

[a] Department of Engineering, University of Campania Luigi Vanvitelli, Via Roma 29, 81031 Aversa, CE, Italy
[b] Department of Civil Chemical Environmental and Materials Engineering, University of Bologna, Via U. Terracini 28, 40131 Bologna, Italy
[c] Department of Industrial Engineering, University of Bologna, Viale del Risorgimento 2, 40136 Bologna, Italy
[d] Department of Enterprise Engineering, University of Rome Tor Vergata, Via del Politecnico 1, 00133 Rome, Italy
[e] CIRTIBS Research Centre, University of Campania Luigi Vanvitelli, Via Roma 29, 81031 Aversa, CE, Italy

ARTICLE INFO

Keywords:
Basalt fibre reinforced composite
Natural fibre
Laser machining
Thermal damage
Interaction mechanisms

ABSTRACT

In the paper, laser cutting of basalt fibre reinforced polymer laminate using a 450 W QCW fiber laser, working in a pulsed regime is presented. Preliminary tests were performed on a basalt laminate, 1.3 mm in thickness, changing the pulse power (Pp) and pulse duration (D) to find the maximum cutting speed. Then a 3^3 experimental plan was carried out changing the pulse power, the pulse duration, and the cutting speed. The kerf width and the heat-affected zone were measured in the section and on the external surfaces. ANOVA analysis was adopted to assess the process parameters' influence. The interaction mechanisms were found and discussed. From the results, the BFRP laminate appears easy to cut at maximum cutting speeds up to 3500 mm/min. However, thermal damages occur. Kerf geometry and HAZ are mainly affected by the cutting speed, while the Pp and D seem to have a minor role.

1. Introduction

Basalt fibres are high-tech fibres produced by the continuous spinning of natural volcanic basalt rock at about 1500 °C. These fibres, and their production process, were developed by the Moscow Research Institute of Glass and Plastic, and first produced in the middle 1980s by the Ukraine fibre laboratory [1]. Nowadays, these reinforcements are adopted for the production of different structural and electro-technical components in different industrial fields, such as bridge/building construction (directly embedded in the masonry or under the form of composite rods or plates) [2–6], anti-ballistic armours [7], fan blades, boats, cars, sports equipment, and household appliance components [8–12].

Although the mechanical, chemical and physical properties depend on the chemical composition of the raw material, basalt fibres show good mechanical properties (ranging between E- and S2-glass) [13–16], service temperatures [17,18], corrosion resistance [19], and excellent physical and chemical properties [16,20–22]. These properties can be modified by hybridization with other reinforcement [23,24], by selecting a suitable matrix (thermosetting or thermoplastic) [25,26] or by surface treatments [27,28]. In addition, since basalt fibres, compared to glass fibres, require less energy and no additives for their production, and they can be easily processed by adopting conventional processes and equipment, they show a potential advantage in cost too [12]. Although basalt fibres show softening and melting temperatures higher than glass fibres, they present lower fire resistance because when exposed to heat flux, basalt fibres heat faster and reach higher temperatures than glass fibres due to their highest emissivity [29]. Moreover, due to the resin-fibre interface issues, basalt fibres may suffer a significant reduction in mechanical properties when subject to alkali exposition [30–32].

A further issue regards the possibility of having low-cost, high-productivity, and sustainable manufacturing processes able to drill, trim and cut BFRP laminate. Like all composite materials, even BFRPs present several issues with conventional drilling/cutting methods, resulting in tool wear, fibre pull-out, delamination, and matrix degradation [33–35].

Among non-conventional technologies, abrasive water jet (AWJ) and laser machining (LM) are known for their ability to machine any kind of material. Compared to the conventional methods, abrasive water jet (AWJ) machining shows different advantages such as the absence of heat affected zone (HAZ), the elimination of dust by jet-entrainment, and high cutting speed absence of wear, it does not require complex fixtures [36]. However, AWJ shows some drawbacks such as moisture

* Corresponding author.
E-mail address: claudio.leone@unicampania.it (C. Leone).

https://doi.org/10.1016/j.compositesa.2023.107800
Received 20 January 2023; Received in revised form 1 September 2023; Accepted 16 September 2023
Available online 17 September 2023

Table 1
Comparison between the main properties of basalt and glass fibres [8,62].

Characteristic	Unit	Basalt	Glass
Colour	–	Light brown	White transparent
Filament diameter	μm	17	7
Density	kg/dm^3	2.8	2.54
Tensile strength	MPa	4800	3200
Elastic modulus	GPa	90	70
Elongation at break	%	3.15	4.0
Max. service temperature	°C	650	460

Table 2
SX8 EVO matrix properties [63].

Characteristic	Unit	Matrix
Tensile strength (ASTM D 638)	MPa	65–75
Elongation at break (ASTM D 638)	%	6–7
Tensile Young's modulus (UNI5819)	GPa	2.4–3.0
Flexural strength (ASTM D 790)	MPa	95–110
Flexural modulus (ASTM D 790)	GPa	2.4 – 3.2
Compressive strength (UNI 4279)	MPa	90–110
Glass transition temperature	°C	75–85
Water absorption 24 h @ room temperature (ASTM D570)	%	0,1–0,2
Water absorption 2 h at 100 °C (ASTM D570)	%	0,6–0,7
Operating temperature	°C	90

absorption, delamination, abrasive particle deposit (for AWJ), and slow effective cutting speed [36–38]. Ramraji et al [39] have studied the effect of process parameters and fly ash content (5–20% wt) during AWJ machining of BFRP laminate. The investigated process parameters were the hydraulic pressure (150–300 MPa), the stand-off distance (1.5–3 mm) and the cutting speed (125–225 mm/min). The kerf taper and the surface roughness were adopted as a quality index. It was observed that increasing jet pressure intensity reduces the fibre pull-out and damage, while the surface smoothness and roughness are affected by the fly ash content. In [40] Ramraji et al. carried out a comparative study on AWJ cutting of both glass and basalt laminate. They conclude that the most significant control factor is the water jet pressure since it affects the surface quality and kerf taper of both materials. However, the kerf deviation is higher for the BFRP, since the latter shows a more brittle behaviour. In addition, the low level of cutting speed, and stand-off distance improve the workability of the two composites. Amuthakkannanat et al. [41] studied the effect of pressure, cutting speed and stand-off distance on the kerf geometry and the delamination extension during AWJ cutting of BFRP 3 mm in thickness. They adopt the Grey Relational Analysis (GRA) to study the effect of the process parameters and to optimise the process conditions. They found that water pressure and stand-off distance affect the kerf formation, while the cutting speed does not significantly affect the kerf characteristics. However, kerf width and delamination in the range of 1.4–1.7 mm and 0.7–1 mm were observed, respectively. Sathishkumar et al [42] studied the effect of traverse speed, stand-off distance and abrasive mass flow of Garnet abrasive (mesh size 80 and grit size of 0.18 mm) on the material removal rate (MRR), the roughness and kerf tapper during the cutting of a hybrid Basalt–Kevlar–Glass laminate, 8 mm in thickness. Analysis of variance (ANOVA) and response surface methodology (RSM) were adopted to find the optimal process condition. They found that good machinability

Fig. 2. Image of the experimental setup.

Table 3
Laser system characteristics.

Characteristic	Symbol	Units	Value
Wavelength	λ	nm	1070 ± 5
Mode of Operation		–	CW/PW
Nominal average power	Pavg	W	450
Max. pulse power	Pp	W	4500
Max. pulse energy	Ep	J	45
Pulse duration	D	ms	0,05 ÷ 50
Modulation frequency	f	kHz	0–50
Beam Parameter Product	BPP	mm × mrad	2–3
Power stability	–	%	±0.5
Output fibre core diameter	–	μm	50
Focal length of the collimator	–	mm	85
Focal length of the focusing lens	–	mm	100
Focussed spot diameter	d	μm	80
Power consumption (@ max Pa)	–	kW	1.8

Table 4
Factors and levels adopted for the experimental plan.

Control factor	Symbol	Unit	Levels		
			−1	0	+1
Pulse power	P_p	kW	3.00	3.75	4.50
Pulse duration	D	ms	0.05	0.15	0.25
Cutting speed	S	mm/min	1800	2100	2400

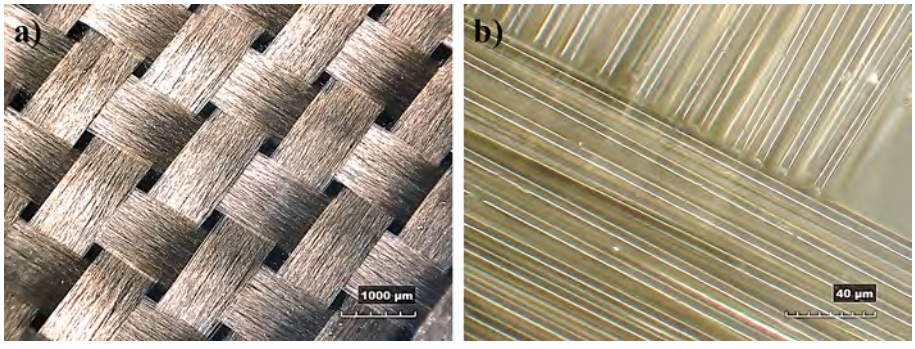

Fig. 1. Images of the reinforcement at different magnifications: a) 50X; b) 1500X.

Table 5
Corresponding process conditions in terms of P_p, D, f, E_p, S, R, and linear energy (Le).

P_p [kW]	D [ms]	f [Hz]	Ep [J]	S [mm/min]	Rt [%] *	Rf [%] **	Le [J/mm]
3	0.05	3000	0.15	2400	86.67	94.94	0.188
				2100	85.42	94.52	0.214
				1800	87.50	96.53	0.250
	0.15	1000	0.45	2400	50.00	84.66	0.188
				2100	56.25	86.07	0.214
				1800	62.50	89.56	0.250
	0.25	600	0.75	2400	16.67	66.17	0.188
				2100	27.08	71.22	0.214
				1800	37.50	82.16	0.250
3.75	0.05	2400	0.19	2400	79.17	91.38	0.188
				2100	81.77	93.81	0.214
				1800	84.38	95.29	0.250
	0.15	800	0.56	2400	37.50	74.62	0.188
				2100	45.31	79.46	0.214
				1800	53.13	85.05	0.250
	0.25	480	0.94	2400	−4.17	59.44	0.188
				2100	8.85	68.90	0.214
				1800	21.88	70.32	0.250
4.5	0.05	2000	0.23	2400	75.00	91.40	0.188
				2100	78.13	91.94	0.214
				1800	81.25	94.35	0.250
	0.15	667	0.68	2400	25.04	71.27	0.188
				2100	34.41	79.65	0.214
				1800	43.78	82.50	0.250
	0.25	400	1.13	2400	−25.00	50.19	0.188
				2100	−9.38	61.61	0.214
				1800	6.25	71.66	0.250

*Theoretical value obtained by imposing ds = 80 μm in eq. (6).
*Value obtained by imposing ds = footprint (Uk)

was achieved at a cutting speed of 200 mm/min, an abrasive mass flow rate of 150 g/s, and a stand-off distance of 3.51 mm. In all cases, irrespective of the laminate thickness, the hydraulic pressure and stand-off distance, the adopted cutting speed does not exceed 300 mm/min. Furthermore, AWJ often produces a kerf width that is on the order of a millimetre. Then there are evident limitations for actual industrial applications of AWJ.

A possible alternative to the AWJ is represented by laser cutting (LC), which can be used on almost all categories of materials, including metals [43–47], ceramics [48], and composites [36,49–51]. Compared to AWJ, laser cutting offers additional advantages: it does not apply any mechanical force; since the laser beam spot is very small, narrow kerfs are produced. In addition, it is possible to achieve a higher material removal rate and, then, a high cutting speed and production rate [38,52]. However, since laser machining is a thermal process, thermal damage and heat affected zone (HAZ) extension are the major issues. As a matter of fact, compared to laser processing on traditional materials, those on composite materials have an evident gap and, the interest of the researcher in laser applications is confirmed by numerous scientific publications and their growth in the last years. In addition, laser cutting of composites reinforced with basalt fibre is scarcely studied. In the last year, Gautam and Mishra have studied the laser cutting of both pure basalt and hybrid (Kevlar-29/basalt) laminate by means of a pulsed 250

Table 6
Response variables nomenclature.

Measuring position	Response variables	Symbol	Unit
Upper surface	Kerf width	Uk	μm
	Average side-to-side HAZ	HAZ_U	μm
	Max side by side HAZ	HAZ_U max	μm
Bottom surface	Kerf width	Bk	μm
	Average side-to-side HAZ	HAZ_B	μm
	Max side to side HAZ	HAZ_B max	μm
Section	Upper kerf width	Uk_S	μm
	Bottom kerf width	Bk_S	μm
	Side HAZ	HAZ_S	μm
	Side to side HAZ	HAZ_S max	μm

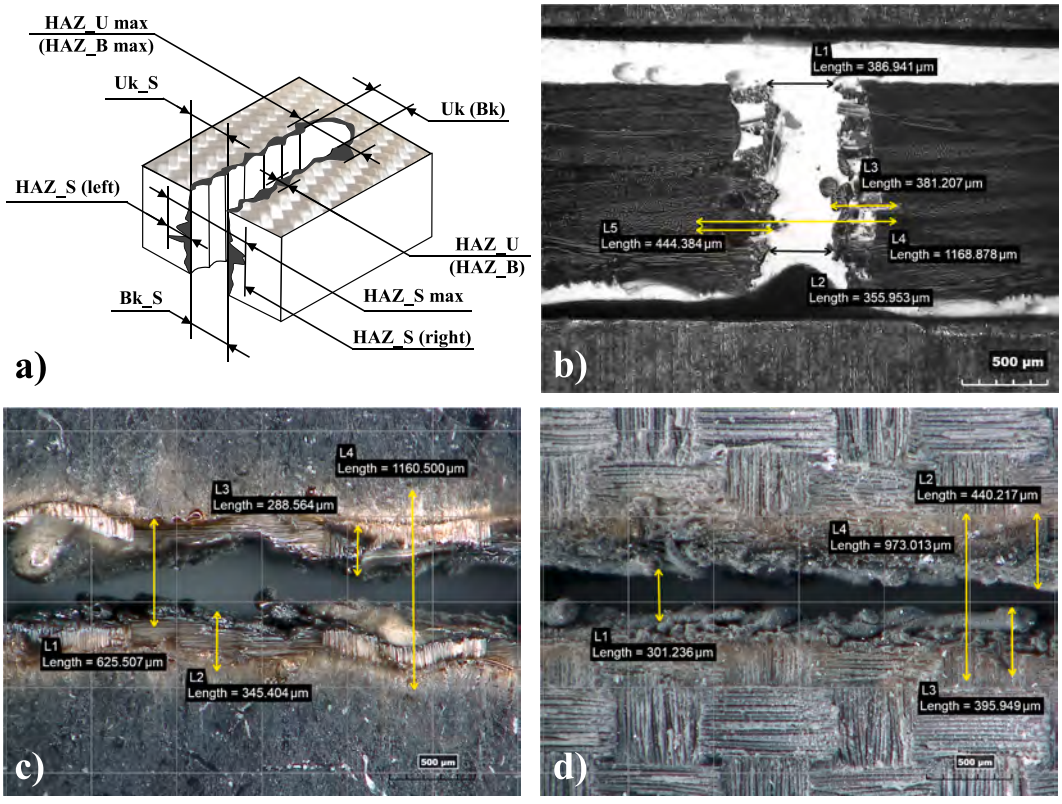

Fig. 3. Schematic of measurement for the kerf geometry and HAZ characterisation. (Cut obtained at S = 2100 mm/min, Pp = 3 kW, D = 0.05 ms).

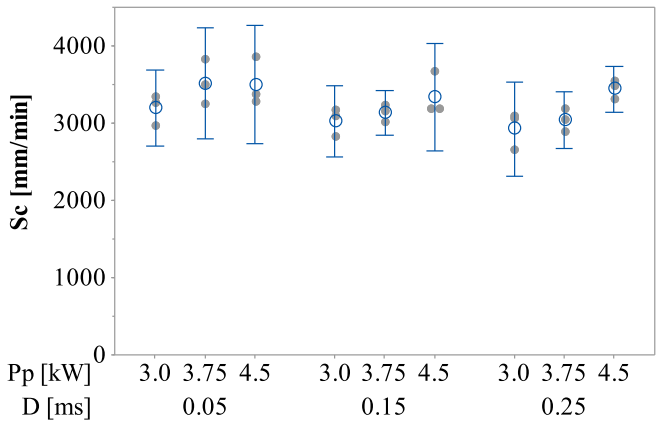

Fig. 4. Individual plot of the maximum cutting speed. In the figure, the empty circles indicate the average value, the filled circles are the punctual values, and the vertical bars indicate the standard deviations.

Table 7
Average value and standard deviation of the maximum cutting speed (Sc) [mm/min].

	Pp [kW]		
D [ms]	3.00	3.75	4.50
0.05	3194 ± 199	3520 ± 292	3502 ± 310
0.15	3029 ± 185	3134 ± 116	3345 ± 280
0.25	2927 ± 246	3039 ± 149	3447 ± 119

Table 8
ANOVA table for maximum cutting speed (Sc).

Source	DF	Adj SS	Adj MS	F-value	*p*-value
D [ms]	2	385033	192516	3.90	**0.039**
Pp [kW]	2	653404	326702	6.62	**0.007**
D*Pp	4	151484	37871	0.77	0.560
Error	18	888669	49371		
Total	26	2078590			

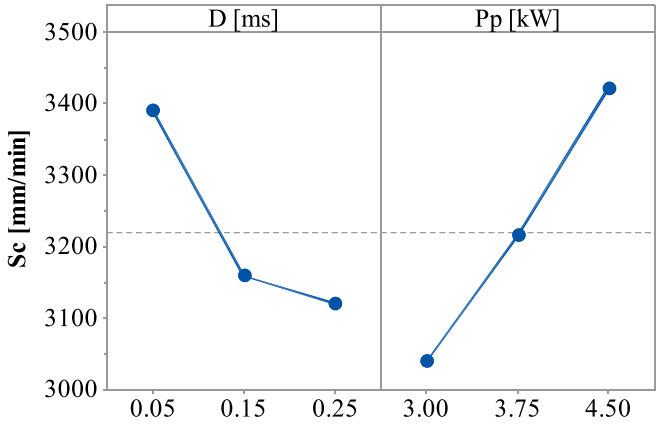

Fig. 5. Main effect plot for maximum cutting speed (Cs).

W pulsed Nd:YAG laser source [53–55]. They adopt different methodologies (Analysis of Variance, Response Surface Methodology, Teaching learning-based optimization, and Firefly Algorithms), for the modelling and optimisation of the process parameters to obtain a regular kerf geometry (narrow and straight kerf, with minimal kerf deviation). During the studies they change the Lamp current (160–200 A), pulse width (2–2.6 ms), pulse frequency (20–30 Hz), air pressure (8–10 Bar) and

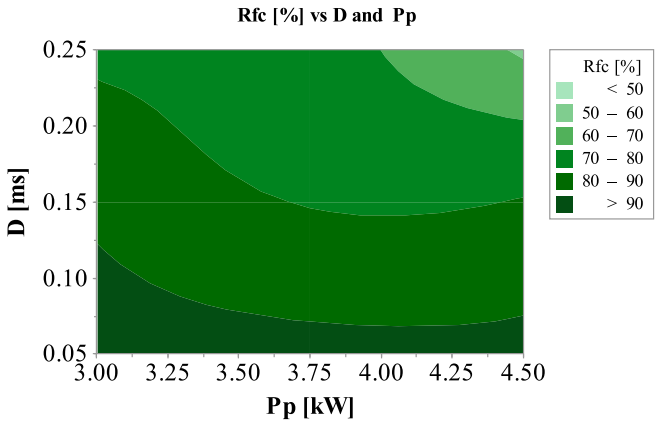

Fig. 6. Effect of pulse power and duration on Rfc.

cutting speed (50–300). Jain et al. [56] carried out a study on laser cutting of basalt-glass hybrid composite adopting similar equipment and process parameters. In this case, the kerf geometry was optimised by adopting Artificial Neural Network (ANN) techniques, irrespective of the thermal damage. Najjar et al. [57] use ANN to estimate the kerf geometry during laser cutting of basalt fibre laminate 1.6 mm in thickness. They adopt a pulsed Nd:YAG laser, changing cutting speed (50–200 mm/min), gas pressure (8–10 Bar), the lamp current (160–200 A), the pulse frequency (20–30 Hz) and the pulse length (2–2.6 ms). Response surface methodology and box-Behnken design were adopted to design the experimental plan. They found that ANNs are able to model the process. Moreover, a narrow kerf with minimum deviation can be obtained by adopting moderate lamp current, high pulse width, high pulse frequency, low air pressure and low cutting speed. Although the efforts spent in the modelling and optimisation of laser cutting of pure basalt and basalt hybrid laminate, the thermal damage formation, modelling, and optimisation were not thoroughly investigated. In addition, the adoption of pulsed Nd:YAG laser, shows some critical issues such as the limited pulse frequency that does not allow the achievement of sufficient overlapping at high speeds (the maximum cutting speed, 300 mm/min, is comparable to the AWJ ones), the difficulty of obtaining the average nominal power in all process conditions (since it depend on lamp current, pulse frequency and pulse duration setting) that does not help in cutting speed increasing, low beam quality and asymmetrical energy distribution, the latter produces variable performance according to the cut direction [43,44].

In recent years, quasi-continuous wave (QCW) fiber lasers, thanks to their specific characteristics, have replaced Yb:YAG lasers source in several applications [58,59]. Compared to pulsed Yb:YAG laser, QCW fiber lasers show several advantages, such as high-quality beam and small focusing diameter, wall-plug efficiency, reliability, zero maintenance, stability, high pulse power, the possibility to have the same average power in a large range of laser parameters [60].

Since laser machining of pure BFRP hasn't been systematically studied, and, compared to pulsed Yb:YAG laser sources, QCW fiber laser offers several advantages, the study of laser cutting of BFRP laminate adopting the aforementioned source has a good research significance. Then, the present paper aims to study the laser cutting process of basalt fibre laminates. To this end, BFRP plates, 1.3 mm in thickness, were produced by resin infusion. Preliminary cutting tests were performed adopting a 450 W QCW fiber laser changing the pulse power and pulse duration, to find the maximum cutting speed. Then a 3^3 experimental plan was developed and carried out, changing the pulse power, the pulse duration, and the cutting speed. The kerf width and the heat affected zone (HAZ) were measured in the section and on the external bottom and upper surfaces. ANOVA analysis was adopted to assess the influence of the process parameters. The interaction mechanisms were analysed and discussed too. From the results, the BFRP laminate appears

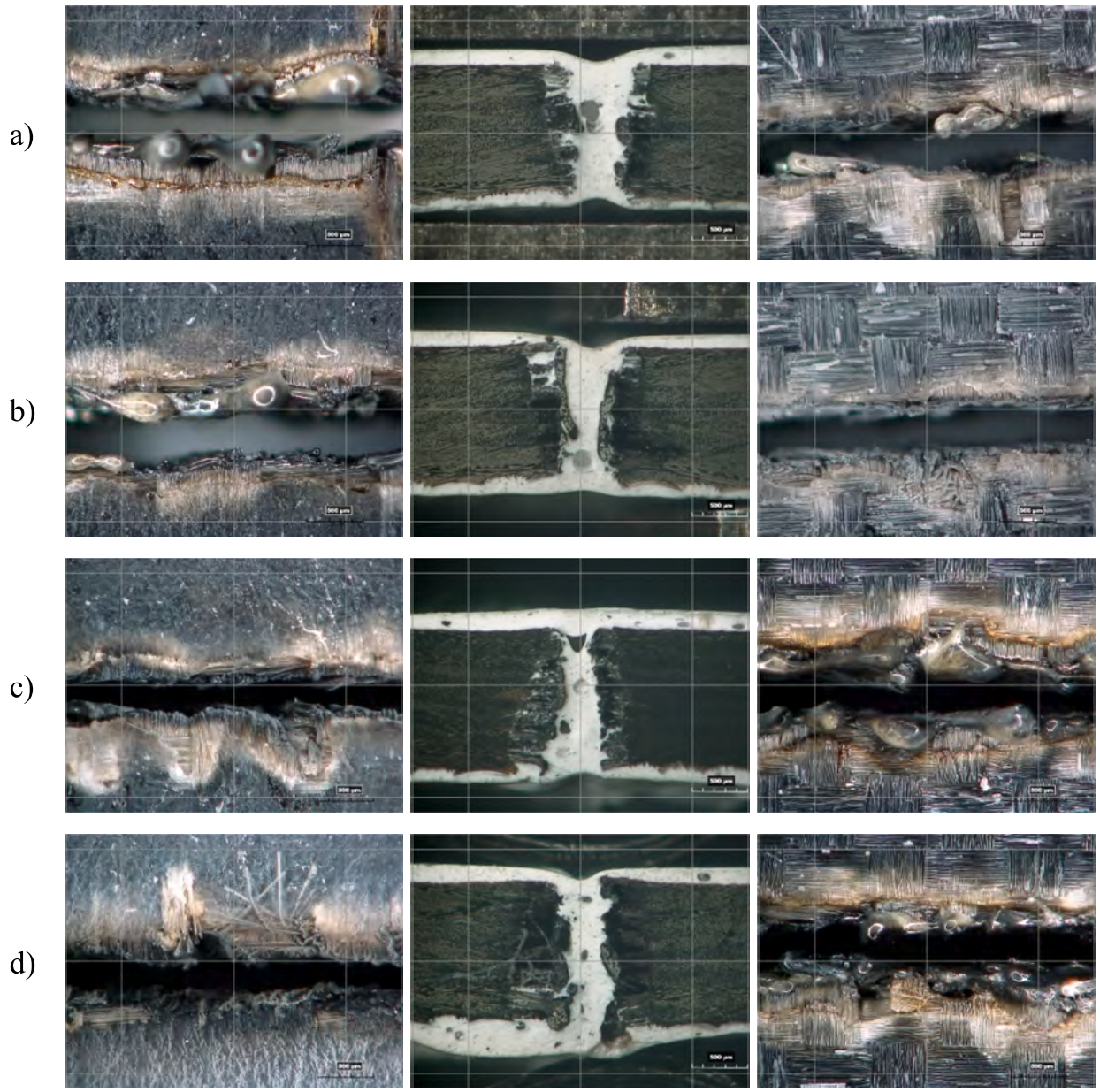

Fig. 7. Images of the upper, section, and bottom kerf obtained at S = 1800 mm/min and: a) *P*p = 3.0 kW, *D* = 0.05 ms; b) *P*p = 3.0 kW, *D* = 0.25 ms, c) *P*p = 4.5 kW, *D* = 0.05 ms, *d) P*p = 4.5 kW, *D* = 0.25. In the figure, the upper surfaces are on the left.

relatively easy to cut, with cutting speeds that can easily reach 2400 mm/min. Thermal damages in the form of matrix burning and recession, fibre protrusion or the presence of a coating made of a mixture of remelted basalt and carbonised matrix were observed. Kerf geometry and HAZ extension are affected by the cutting speed and the molten basalt flow produced inside the kerf. The effect of measurement position was analysed and discussed too.

2. Materials, equipment, and experimental procedures

2.1. Material

The cutting tests were performed on a BFRP laminate 300 × 240 mm^2 in-plane dimension and 1.32 ± 0.02 mm in thickness produced by resin infusion, according to the procedure described in [61]. As reinforcement materials, 8 plays of basalt dry fabrics, 200 g/m^2, plain-weave (warp 10F/10 mm, weft 10F/10 mm), and tex 100, from ZLBM (De), were adopted. The stacking sequence was $[(0/90)_2\ (\pm45)_2]_s$. A 2-component modified epoxy system (Mates SX8 EVO mixed with slow hardener) was adopted for the matrixed. This kind of resin is a low-viscosity matrix specifically developed for injections, infusions, and RTM processes. In Table 1 and Table 2 the basic properties of the basalt fibres and the epoxy matrix, as declared by the producers, are reported, respectively. While in Fig. 1 images of the adopted reinforcements at different magnifications are reported. After, the plate production, stripes, 260 × 40 mm^2, were obtained by diamond saw cutting and adopted for the laser cutting tests.

2.2. Equipment

Cutting tests have been performed on a commercial 3 + 1 axis CNC system (Rofin finecut Y340M) equipped with a 450 W Quasi-Continuous Wave (QCW) Yb:YAG fiber laser source (IPG YLR-450, 4500-QCW-MMAC-Y14) emitting at 1070 nm wavelength with a quasi-Gaussian intensity distribution. The laser source has a nominal average power (Pavg) of 450 W in both continuous wave (CW) and pulsed wave (PW)

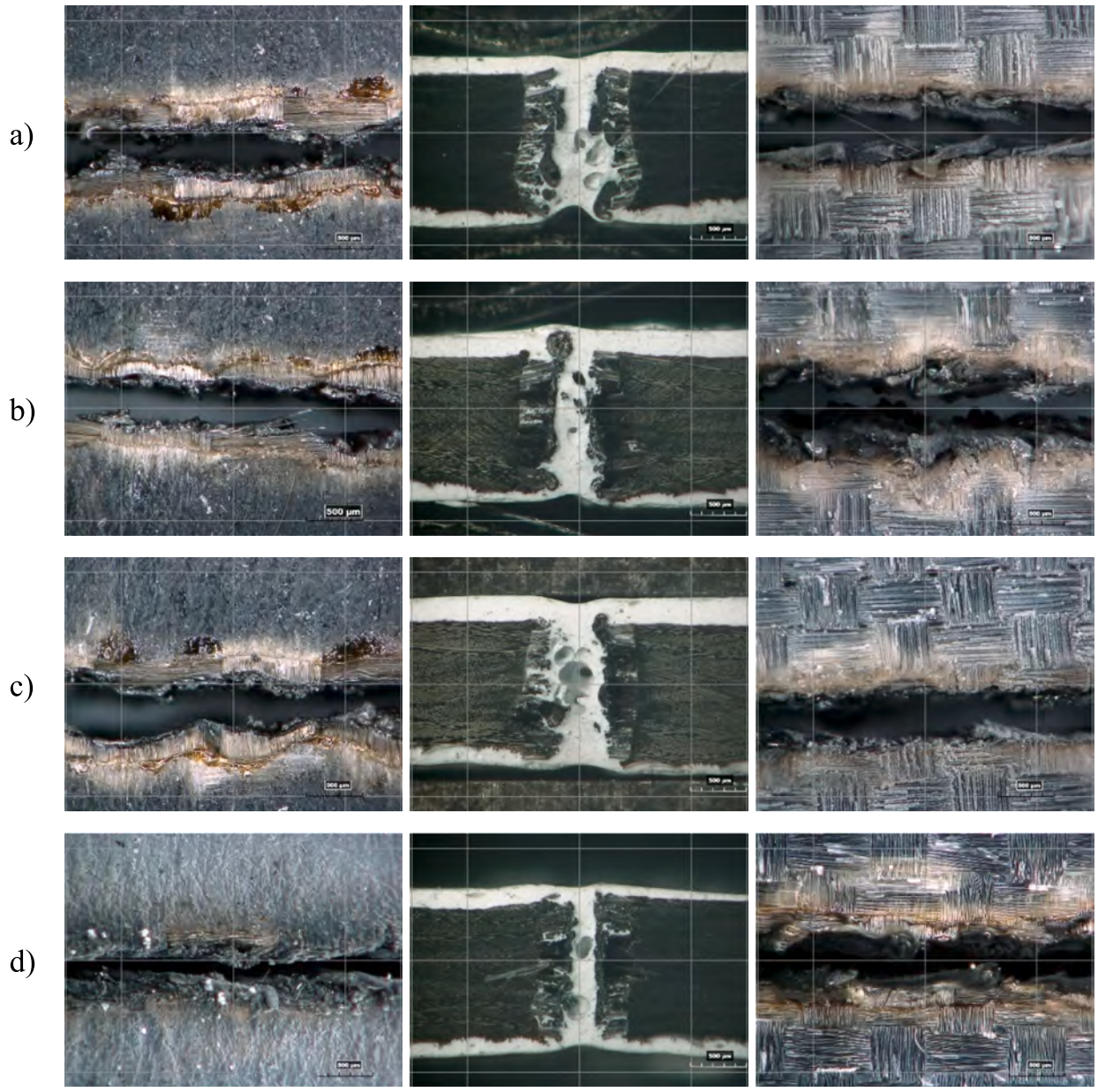

Fig. 8. Images of the upper, section, and bottom kerf obtained at S = 2400 mm/min and: a) *P*p = 3.0 kW, *D* = 0.05 ms; b) *P*p = 3.0 kW, *D* = 0.25 ms, c) *P*p = 4.5 kW, *D* = 0.05 ms, *d) P*p = 4.5 kW, *D* = 0.25. In the figure, the upper surfaces are on the left.

regimes. In the latter case, the pulse power (Pp) can reach values up to 4500 W, with the following limitation: the average power cannot exceed the nominal value in CW mode (450 W) and the duty cycle (δ) (i.e. the product of the frequency per pulse duration) cannot exceed 50%. Considering the well-known equations for the average power, pulse energy (E_p), pulse power, and duty cycle (δ) [52,60]:

$$E_p = Pavg/f \tag{1}$$

$$P_p = \frac{E_p}{D} \tag{2}$$

$$\delta = 100f{\cdot}D \tag{3}$$

Where Ep, Pp, f, and D are the pulse energy, the pulse power, the pulse frequency, and the pulse duration, respectively. Then, considering the source limitation, in the PW mode, the following constraints must be observed:

$$f{\cdot}D \leq 0.5 \tag{4}$$

$$Pavg = Pp{\cdot}f = \left(\frac{E_p}{D}\right){\cdot}f \leq 450 \tag{5}$$

The laser beam has been delivered through a 50 µm core optical fibre into a cutting head (IPG Micro Cutting Head P21-010105 D25), equipped with an 85 mm collimation lens and a 100 mm focusing lens. The beam parameter product (BPP), as declared by the producer, is 2.4 mm × mrad, corresponding to a M^2 factor of about 7 and a theoretical beam diameter at the focussing point of about 80 µm. In Fig. 2 an image of the experimental setup is reported, while in Table 3 the main characteristics of the laser are summarised.

2.3. Experimental procedures

The experimental tests were developed according to the Design of Experiment (DoE) methodology. This approach includes the selection of

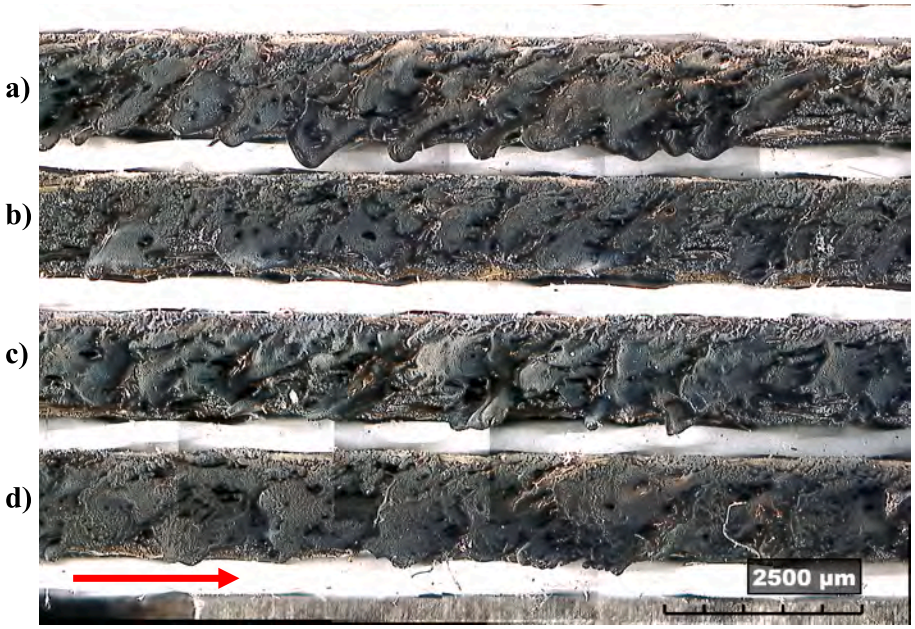

Fig. 9. Images of the kerf's walls obtained at S = 1800 mm/min and: a) *P*p = 3.0 kW, *D* = 0.05 ms; b) *P*p = 3.0 kW, *D* = 0.25 ms, c) *P*p = 4.5 kW, *D* = 0.05 ms, *d) P*p = 4.5 kW, *D* = 0.25. In the figure, the arrow indicates the travel direction of the laser beam.

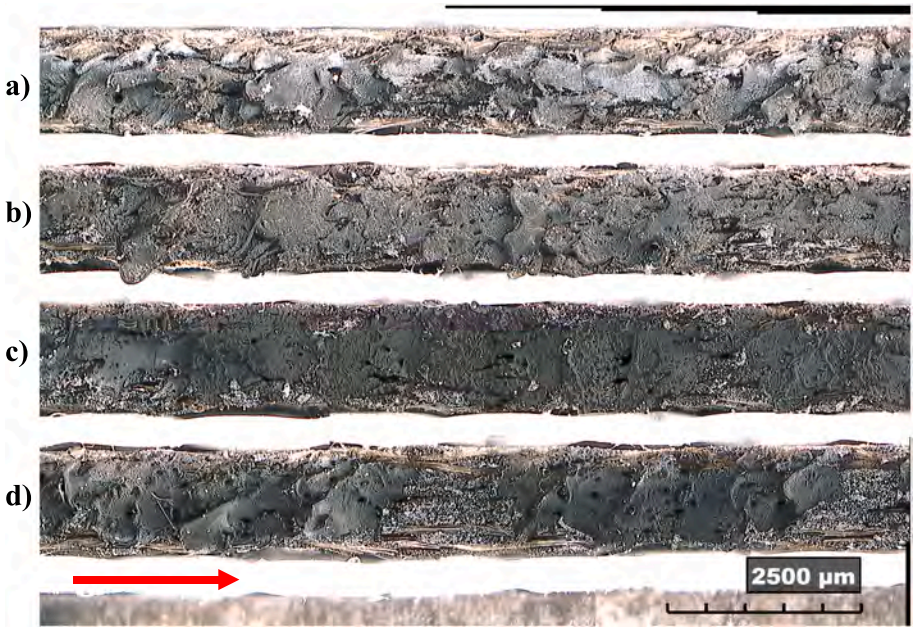

Fig. 10. Images of the kerf's walls obtained at S = 2400 mm/min and: a) *P*p = 3.0 kW, *D* = 0.05 ms; b) *P*p = 3.0 kW, *D* = 0.25 ms, c) *P*p = 4.5 kW, *D* = 0.05 ms, *d) P*p = 4.5 kW, *D* = 0.25. In the figure, the arrow indicates the travel direction of the laser beam.

the experimental plan as well as the control factors (i.e. the settable process parameters that affect the cutting process), their levels (values), and the response variables (the measured quantity that describes the process behaviours). As a matter of fact, for a pulsed laser source, there are several possible control factors, excluding the material characteristics that are fixed, they are the average power (Pavg), the pulse power (P_p), the pulse duration (D), the pulse frequency (f), the overlapping percentage (R%), that is the percentage of the overlap between two consecutive pulses, the cutting speed (S), the focusing position, the stand-off distance (SOD), the type of assistant gas and its pressure.

The use of too many variables involves a large number of tests to be performed. Also, the selection may be complex since some of these quantities are derived from each other (see Eqs. 1–3). Then, to reduce the number of tests and focus on the process and laser system parameters, some factors were fixed according to the following consideration: since the thickness of the laminate (1.3 mm) is in the same order as the focussing depth (i.e. the Rayleigh length), it was decided to fix the focus position on the sample surface, the SOD was fixed at the standard value for the adopted head (1 mm), to avoid combustion phenomena (due to O_2 presence) and/or excessive erosion (produced by too-high pressure), as assistance gas, nitrogen at a pressure of 0.7 MPa was adopted, according to the results obtained in [64], finally, to assures highest performances in term of achievable cutting speed the average power was fixed at the maximum values (450 W).

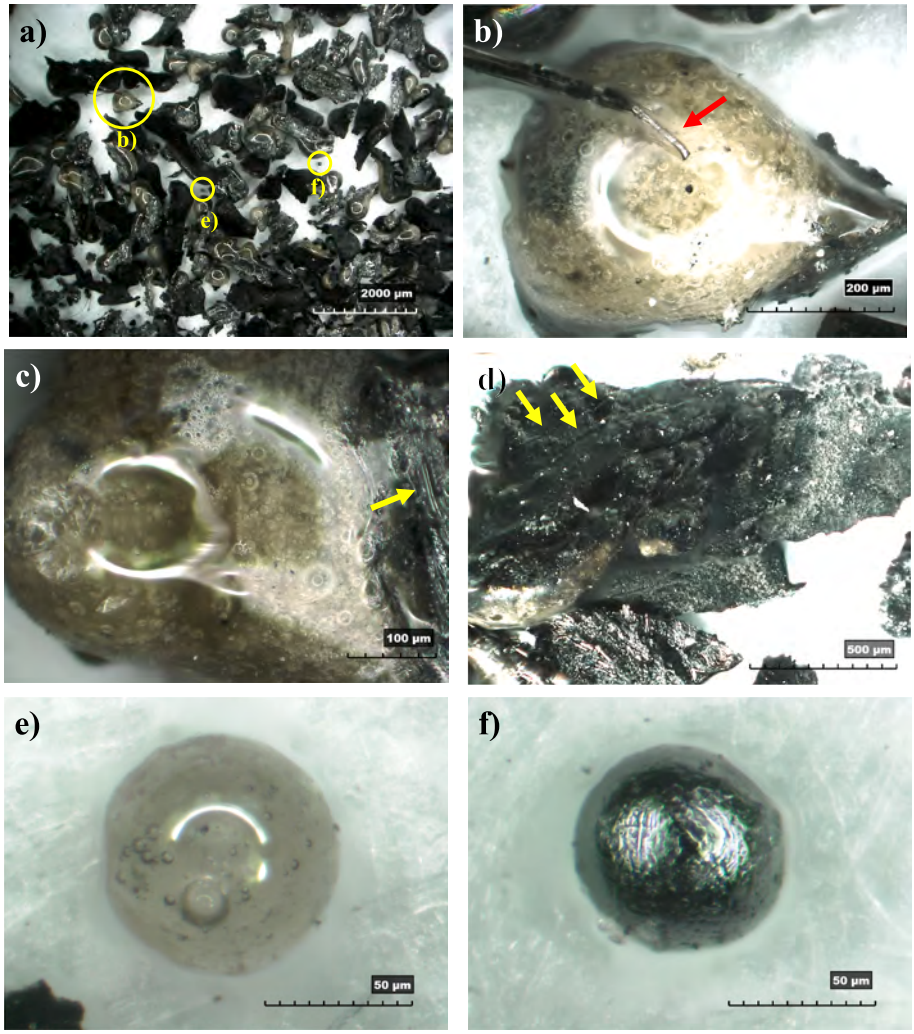

Fig. 11. Selected images of the debris separated from the kerf wall after cutting. In the figures, the arrow indicates basalt fibres' presence. a) Debris overview; b-c) Large drops of basalt with gas bubble; d) Carbonised matrix fragments and basalt fibre; e) Basalt micro-droplets; f) basalt mixed with the carbonised matrix.

Then, a 3^3 full factorial plan was developed adopting as control factors the pulse power, the pulse duration, and the cutting speed. The selected levels were in the range of 3–4.5 kW; 0.05–0.25 ms and 1800–2400 mm/min, respectively. These values were selected based on the laser characteristics, previous experiences [60,61,65], preliminary tests, and relevant bibliography. In any case, they were chosen to assure the maximum cutting speed and minimum thermal damage. The pulse frequency was obtained according to Eqs. 1–2 imposing Pavg = 450 W. During the experimentation, the tests were replicated three times and fully randomised for each replication.

It is worth noting that pulsed laser cutting involves the overlapping of a series of single footprints each one generated by a single pulse; therefore, to ensure the throughout-cut and good quality of the kerf surfaces, it is necessary that the overlapping is greater than a certain critical value (for metals it is about 70–75%). The overlapping can be calculated by the following:

$$R\% = 100\cdot[1-(S/f)/(ds+S\cdot D)] \approx 100\cdot[1-S/(f\cdot ds)] \quad (6)$$

where ds represents the beam diameter at the focussing point (Rt) or the beam footprint on the component (Rf). Although the spot overlapping is a significant factor in pulsed laser cutting operation, in the present paper it was preferred to use the cutting speed. This choice was adopted considering that higher values of the overlapping involve component overheating and that, for a QCW laser source, the simultaneous adoption of high Pp and long D imply low frequencies (400 Hz at Pp = 4.5 and D = 0.25 ms, vs. the maximum that is 3000 Hz) that involve low cutting speed (from eq. (4), 5 and 6). Since adopting a low cutting speed could penalize the process in terms of energy consumption, efficiency; process time; and, due to excessive heating, and material damages, it has been chosen to use the cutting speed as a control factor. Therefore, before carrying out the cutting tests, a pre-test campaign was carried out to measure the maximum cutting speed for the different Pp-D combinations. Then cutting speeds of about 80%, 70%, and 60% (2400, 2100, and 1800 mm/min) of the lower maximum cutting speed (about 2900) were adopted for the following tests. The procedure adopted in the pre-tests campaign is described in a following paragraph. Table 4 and Table 5 show the factors and levels adopted in the experimental plant and the corresponding process conditions.

After the tests, the kerf geometries and the thermal damages were first investigated on the external surfaces (at the laser beam input and output); then, to analyse the section, the kerfs were filled with white acrylic paint and then polished using abrasive paper of grit size up to P2500 (Standard ISO 6344).

EN ISO 17658 (Welding - Imperfections in oxyfuel flame cuts, laser beam cuts and plasma cuts – Terminology) and ISO 9013 (Thermal cutting - Classification of thermal cuts - Geometrical product specification and quality tolerances) Standards were adopted to select the response variables. More in detail, the kerf widths in the section were measured at the upper and the bottom of the kerf, UK_S, and BK_S, respectively. To characterise the thermal damage, the heat-affected zone

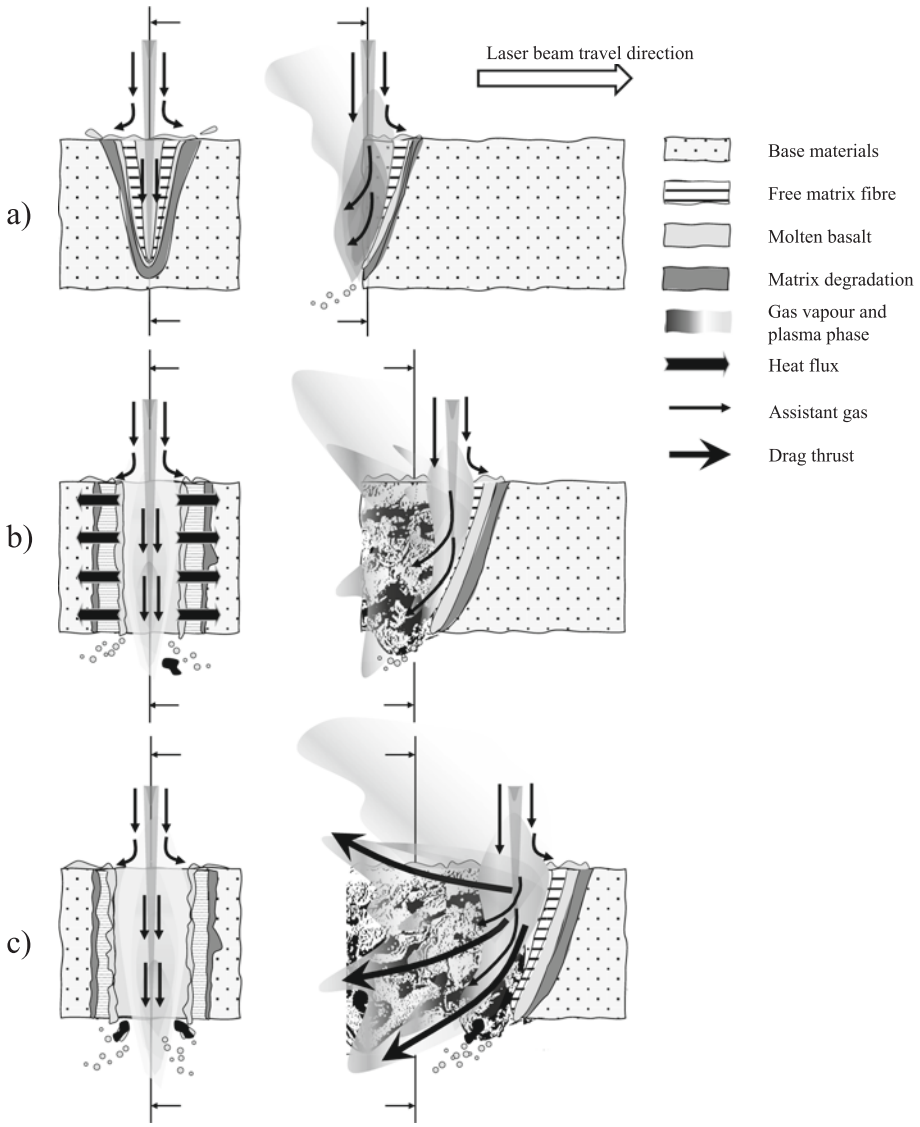

Fig. 12. Schematic of Laser-BFRP interaction mechanisms. a) Cut starting; b) After few cutting mm; c) In regime condition.

extension (HAZ_S) was measured on the left and right kerf sides surface, as proposed by Tagliaferri et al. [66,67], and from side to side (HAZ_S max), as proposed in [60,61,68]. Moreover, since some authors have adopted the measurement of the kerf geometry and the HAZ on the external surfaces [69–71], the value of the kerf widths, the HAZ extension and the side-to-side HAZ, measured on the bottom and upper surfaces have been measured too. A digital microscope (Hirox KH8700) was adopted for the kerf observation and measurement. Some parameters, like the perpendicularity, non-planar cut face, the cut angle, or the roughness, which are further parameters considered in ISO 9013, were not evaluated since the thermal defects greatly exceed these latter.

For each cut, no less than 3 measurements, at a distance of 4 mm, were recorded on the external surface. In Fig. 3 a schematic of the measures is reported; while in Table 6, the response variables' nomenclature is reported. It is worth noting that the texture visible on the bottom surface is the peel ply footprint.

The influence of the test parameters on the kerf geometry and quality was assessed through the ANalysis Of VAriance (ANOVA). This analysis tests the significant differences between the means of the response variables by dividing its total variation into the contribution due to different sources (error, experimental group membership…) and comparing the variance due to the between-groups (or treatments) variability with the one due to the within-group (i.e. the same treatment). During the analysis, a confidence level of 95% ($\alpha = 0.05$) was adopted. It means that a control factor or an interaction is considered statistically significant if the p-value < 0.05. The ANOVA assumes that experiments are independent and normally distributed with equal variances between cutting conditions. Then, before the analysis, these assumptions were checked by the residuals analysis, as suggested in [72,73]. However, this analysis is not reported here for the sake of briefness.

3. Results

3.1. Maximum cutting speed determination

Preliminary tests were performed starting from a cutting speed corresponding to a spot overlap of 75% and increasing the cutting speed with a step of 20% up to observe a no-throughout cut. Then, starting from the highest speed that permits the obtaining of a throughout cut, the procedure was iterated adopting, first a step of 10% and then a step of 5%. The maximum cutting speed obtained with the last iteration was assumed as the maximum cutting speed. To ensure robustness in the maximum speed determination, the last iteration was repeated three

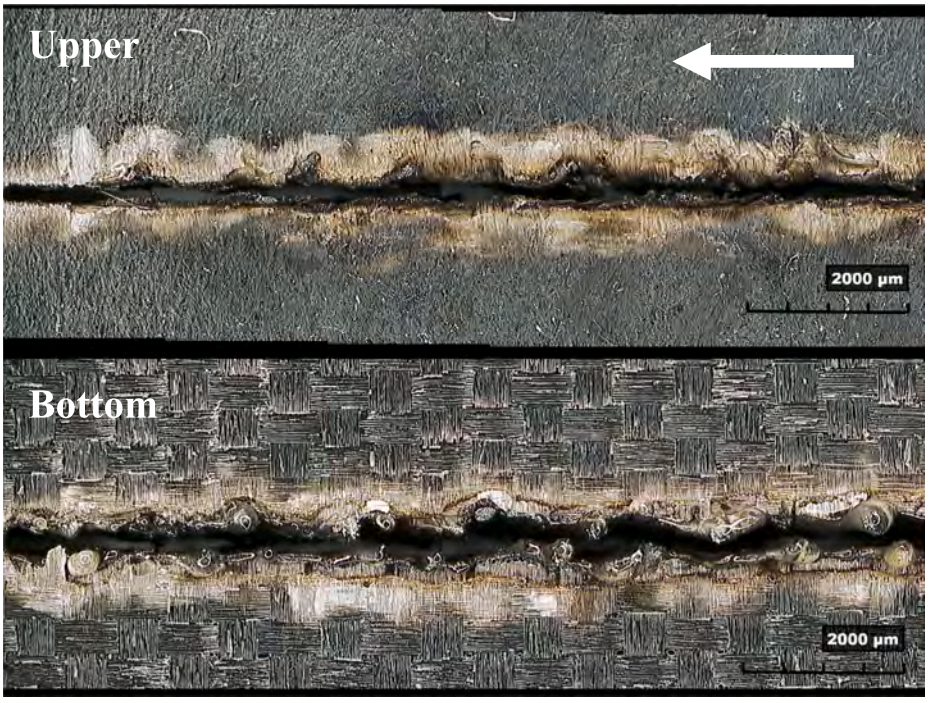

Fig. 13. External surface close to the end of the cut. Sample obtained at S = 2100 mm/min, Pp = 3 kW, D = 0.05 ms. In the figure, the arrow indicates the travel direction of the laser beam.

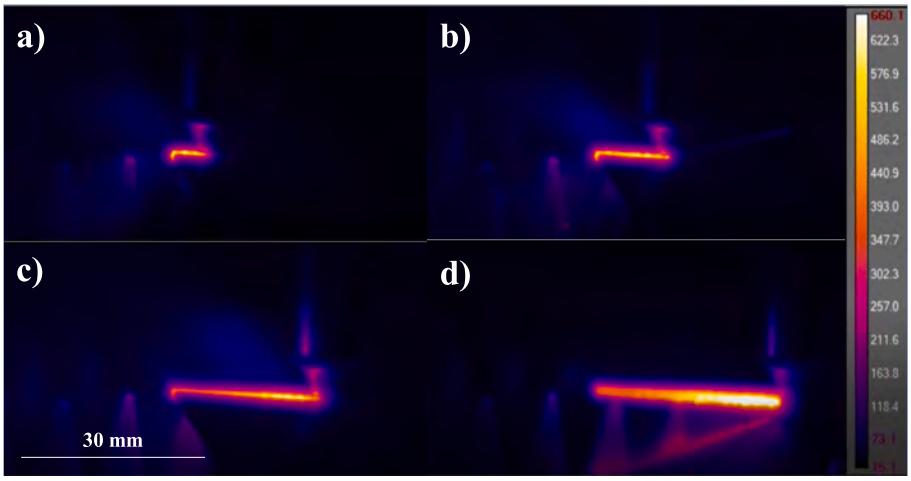

Fig. 14. IR images obtained at Pa = 4.5 kW, D = 0.15 ms, Ss = 2100 mm/s. The images are obtained at; a) about 5 mm from the initial edge, b) in the sample middle; c) near the end of the cut; d) immediately after the cut end.

times obtaining three values of the maximum speed for each test condition.

In Fig. 4 the Individual plot of the maximum cutting speed (Sc) is reported; in the figure, the empty circles indicate the average values, while the vertical bars are the standard deviations. In Table 7 the average values of the maximum cutting speed are reported together with the standard deviation. From Fig. 4, the maximum cutting speed varies from a minimum value of about 2900 mm/min (@ Pp = 3 kW and D = 0.25 ms) to a maximum one of about 3520 mm/min (@ Pp = 3.75 kW and D = 0.05 ms. However, since certain data scattering is observable, the ANOVA was performed to verify the significance of the control factors (Pp and D) and their effects on the maximum cutting speed. In Table 8 the ANOVA results are reported. From the table, both Pp and D are statistically significant (p-value < 0.05). Furthermore, since the F-value of the Pp, compared to the D one, is double, the Pp plays the relevant role in the maximum cutting speed determination; at least, in the analysed parameter range. In Fig. 5 the main effect plot is reported, from the figure, the maximum cutting speed increases at the pulse power increase and vice versa for the duration. It is worth noting that, if the former effect is expected, the reduction of Sc at the increase of the duration, since normally the opposite happens, needs an explanation: increasing the pulse duration, since Pavg is fixed, a decrease of the pulse frequency is needed. Therefore, according to Eq. (6), a decrease in the overlapping is obtained and this results in a reduction of the maximum cutting speed. In other words, the effect of the overlapping is still present and overcomes the effect of the pulse duration.

About the overlapping percentage, it is worth noting that at the maximum cutting speed the theoretical overlapping percentage, Rt (calculated by imposing ds = 80 μm), varies from negative (−79% at Pp = 4.5 and D = 0.25 ms) to positive values (78%, @ Pp = 3 kW and D =

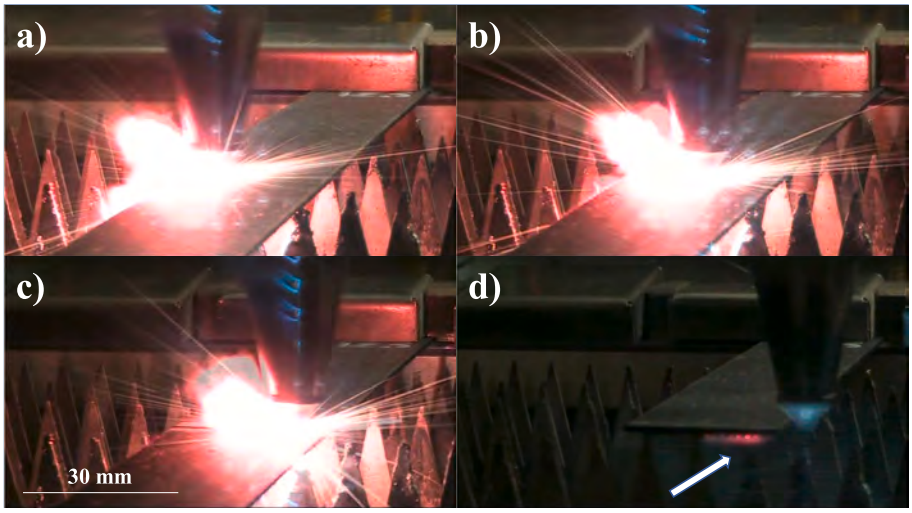

Fig. 15. Images acquired in the visible spectrum at Pa = 4.5 kW, D = 0.15 ms, Ss = 2100 mm/s. The images are obtained at; a) about 5 mm from the initial edge, b) in the sample middle; c) near the end of the cut; d) immediately after the cut end.

Table 9
ANOVA table for the parameters measured in the section.

	Uk_S		**Bk_S**		**HAZ_S**		**HAZ_S max**	
Source	F-value	*p*-value	F-value	*p*-value	F-value	*p*-value	F-value	*p*-value
S	5.48	**0.007**	3.50	**0.036**	2.42	0.097	4.78	**0.012**
Pp	0.81	0.449	1.89	0.159	0.01	0.990	0.10	0.906
D	0.81	0.448	2.35	0.104	0.46	0.632	0.16	0.852
S*Pp	0.41	0.802	0.04	0.996	1.23	0.309	1.39	0.249
S*D	0.31	0.873	0.48	0.751	1.35	0.263	0.46	0.762
P*D	2.02	0.103	0.99	0.422	0.80	0.527	0.77	0.546
R-Sq [%]		35.86%		33.19%		29.71%		30.37%

Table 10
ANOVA table for the parameters measured on the surfaces.

	Uk		**Bk**		**HAZ_U**		**HAZ_U max**		**HAZ_B**		**HAZ_B max**	
Source	F-value	*p*-value	F-value	*p*-value	F-value	*p*-value	F-value	*p*-value	F-value	*p*-value	F-Value	*p*-value
S	9.00	**0.000**	6.25	**0.003**	1.93	0.154	4.61	**0.014**	7.61	**0.001**	7.84	**0.001**
Pp	2.77	0.071	2.28	0.111	0.77	0.466	0.81	0.449	3.61	**0.033**	6.49	**0.003**
D	1.56	0.219	2.94	0.060	0.12	0.890	0.47	0.628	2.54	0.087	1.11	0.337
S*Pp	1.10	0.366	0.43	0.786	1.18	0.327	1.83	0.135	0.20	0.937	0.28	0.888
S*D	0.41	0.799	0.34	0.853	0.91	0.463	0.76	0.555	0.83	0.510	0.40	0.805
P*D	0.54	0.705	0.94	0.447	0.41	0.798	0.33	0.859	1.35	0.262	2.40	0.060
R-Sq	37.97%		68.05%		25.28%		29.37%		51.10%		43.02%	

0.05 ms), where negative values indicate that the laser pulses fall on separate points. While the effective overlapping percentage Rf (calculated by imposing ds = Uk) varies in the range of 42–95%. In Fig. 6 the critical overlapping percentage, (Rfc), that is the Rf value below which there is no through-cut, is reported as a function of Pp and D. From the figure the Rfc decreases increasing Pp and/or D.

This explains why, as a control factor, it was preferred the cutting speed instead of the theoretical R [%]. As a matter of fact, the adoption of Rt or Rf in the order of 70–75% (typical values for metal cutting) would have involved too low speeds adoption, with the consequent increase in the damages due to the overheating. Moreover, a kerf width larger than ds indicates good laser workability of the basalt composite. Furthermore, the adoption of a cutting speed between 60% and 80% of the maximum, in the experimental plan, was necessary to assure thorough cuts. It is worth noting that the values found here are more than an order of magnitude larger than those adopted for AWJ [39–42] or laser cutting [53–57] operations.

3.2. Analysis of kerf characteristics and cutting mechanisms

In Fig. 7 and Fig. 8 images of the upper, the section, and the bottom kerf obtained in different process conditions are reported; while in Fig. 9 and Fig. 10, the kerf walls obtained in the same process conditions are reported too. In Fig. 7 and Fig. 8, the upper surfaces are on the left, while the texture on the bottom surfaces is the peel-ply footprint. These figures show the typical composite material damages due to the laser interaction, such as matrix recession on the external surfaces, the presence of protruded fibres, and matrix degradation (matrix browning) on the upper and bottom surfaces. In addition, at the entrance and exit of the kerf, it is possible to observe the presence of re-solidified drops of molten basalt. Observing the sections profiles, the heat-affected zone consists of three layers: a first layer, external to the kerf wall, with an irregular shape, consisting of black re-solidified basalt mixed with carbon deposits; the second layer is made of fibres without matrix or, more rarely, fibres incorporate in a carbonized matrix; the third one consists of a very thin layer of carbonized matrix. The latter is not always visible/present.

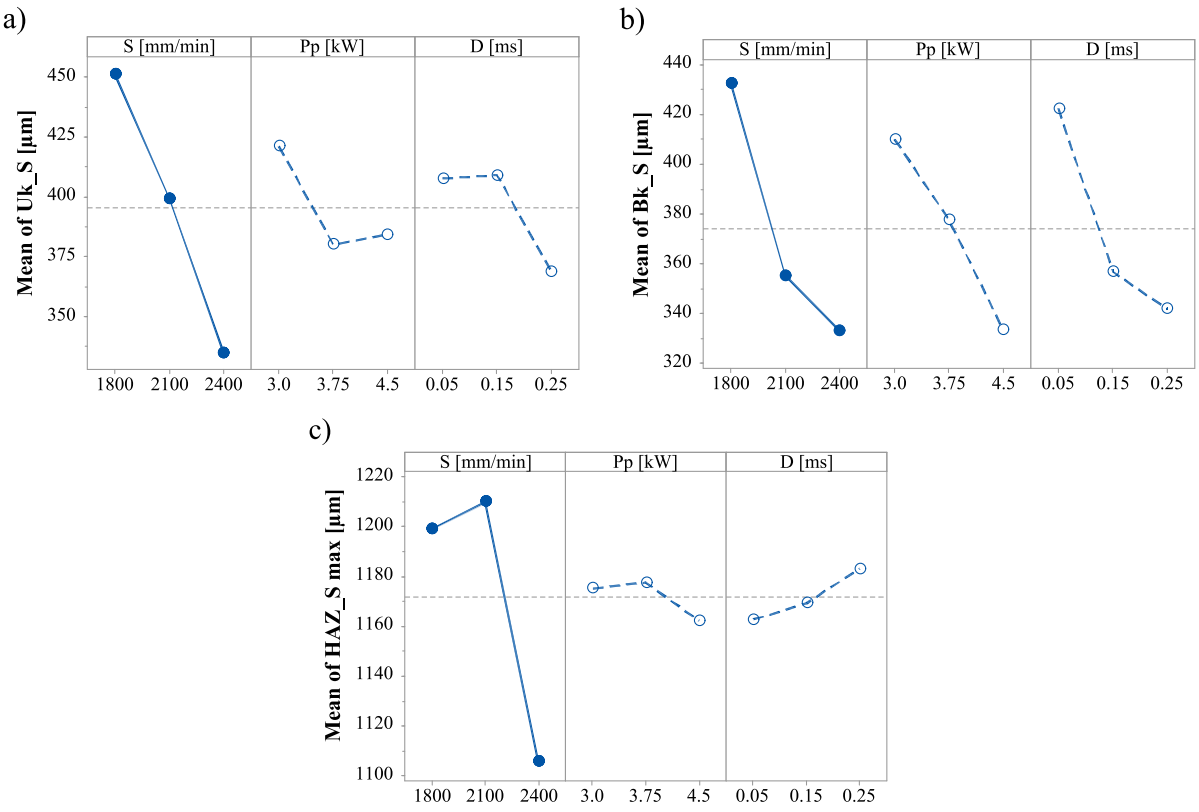

Fig. 16. Main effect plot of the parameters measured in the section: a) Upper kef width; b) Bottom kerf width; c) HAZ extension.

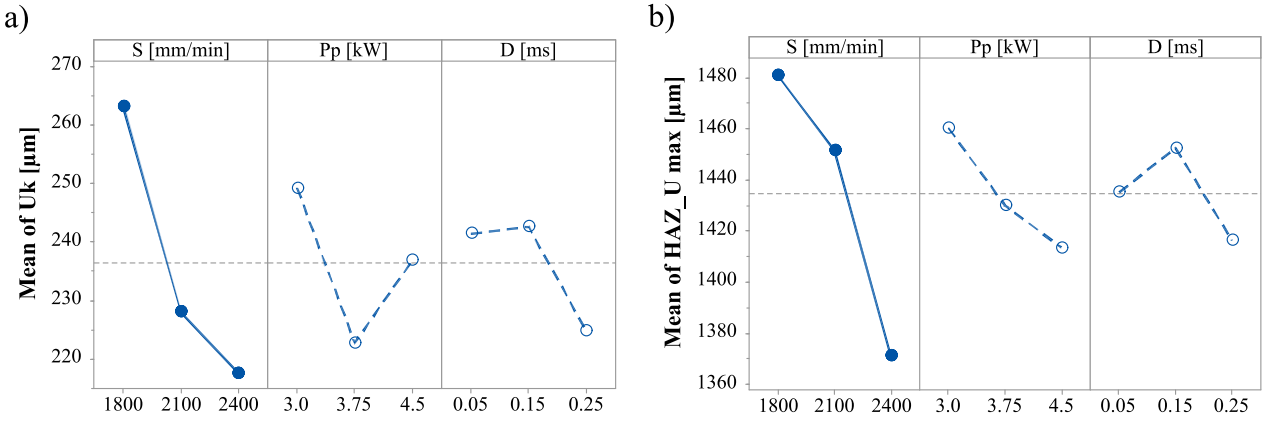

Fig. 17. Main effect plot of the parameters measured on the upper surface: a) Upper kef width; b) HAZ extension.

Observing the walls of the kerf, Fig. 9 and Fig. 10, evident striations can be seen on the first layer. The striations are reminiscent of those produced in the oxygen-assisted laser cutting of steels. The angle of the striations varies from a minimum between 0° and 8° to a maximum of 68°. The layer appears thicker and more remarkable for cuts made at low speed (1800 mm/min, Fig. 9) and less consistent for those obtained at high speed (2400 mm/min, Fig. 10). On the latter, moreover, large areas with uncovered fibres are observed, this is consistent to [54]. Indicates that the outer layer (the first layer) is blown off during the cut itself. This is confirmed by the large quantity of debris and the burr produced during the cutting. Part of them has ejected out of the kerf thanks to the assistance of gas action and the plasma plume, part remains attached to the walls of the kerf forming the first layer and the burr observed at the upper and bottom surfaces. In Fig. 11 some selected images of the debris separated from the kerf wall after the cutting operation are reported. The debris consists of resolidified basalt droplets rich in carbon deposits, drops of only basalt with dimensions considerably larger than the fibres and rich in gas bubbles inside (Fig. 11b and Fig. 11c), carbonised matrix fragments with the fibres still visible inside (Fig. 11d), micro-droplets (about 70 µm in diameter) of basalt or basalt and carbonised matrix, Fig. 11e and Fig. 11f, respectively.

Comparing Fig. 7 and Fig. 8, it is not possible to identify a clear trend of the kerf geometry (shape and width), HAZ extension, and/or striation characteristics. However, there are some qualitative indications: the resolidified droplets on the external surface appear numerous and larger on the bottom surface, especially when the lower cutting speed is adopted, unlike what happens in CFRP laser cutting with the same equipment and under similar conditions [60], the BFRP laminate shows an irregular kerf profile (wavy instead of straight); the kerf section appears more regular for high Pp and D values; conversely, low Pp and D

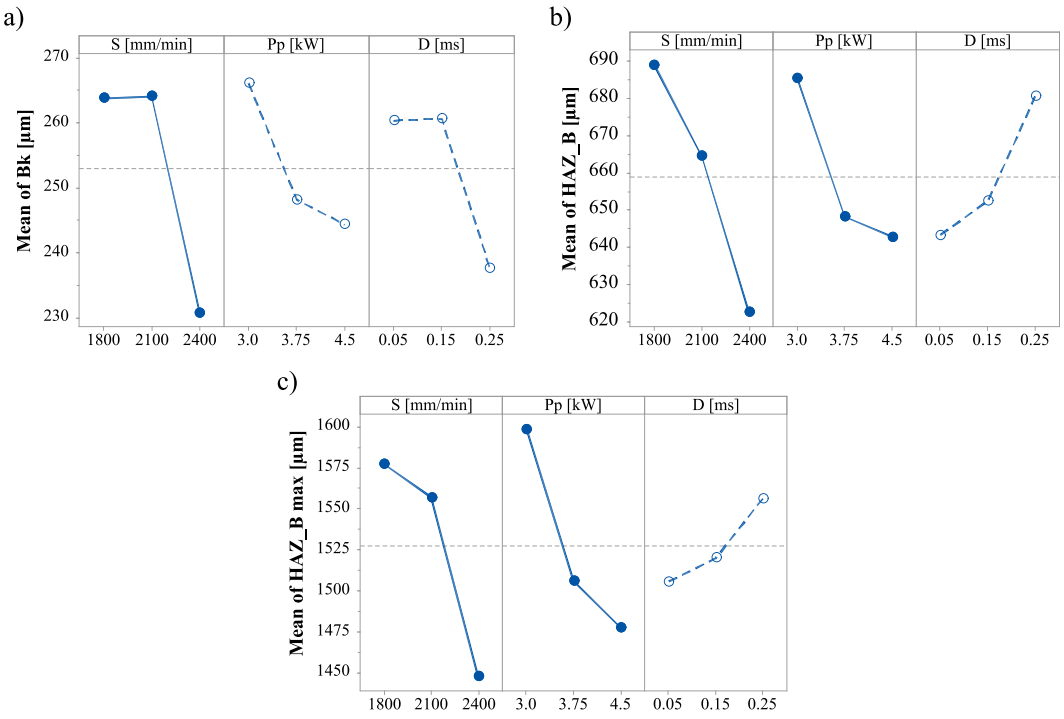

Fig. 18. Main effect of the parameters measured on the bottom surface: a) Bottom kerf width; b) HAZ extension; c) Side to side HAZ.

Table 11
Correlation table between the measurement in the kerf section and on the surfaces (R-Sq [%] values).

	Uk [µm]	Bk [µm]	HAZ_U [µm]	HAZ_U max [µm]	HAZ_B [µm]	HAZ_B max [µm]
Uk_S	**26.2 (s)**	**15.9 (s)**				
Bk_S	**19.51 (s)**	**32.5 (s)**				
HAZ_S			0.01 (ns)	0.24 (ns)	0.45 (ns)	0.02 (ns)
HAZ_S max			2.13 (ns)	3.40 (ns)	3.45 (ns)	2.30 (ns)

s = significant: p-value < 0.05.
ns = not significant: p-value > 0.05.

involve barrel profiles (similar to those observed in [19]). The upper kerf appears more regular when high pulse power and duration are adopted (Fig. 7c and Fig. 8c).

Based on the observations, the interaction mechanism can be summarised as reported in Fig. 12: the laser penetrates the first layer of the matrix and is absorbed by the basalt fibres that melt Fig. 12a); the molten fibres exchange heat with the surrounding matrix, producing the combustion/vaporization of the latter. The vapours produced partly mix with the molten basalt generating the bubble inside the basalt droplets visible in Fig. 11b-c-e, partly forming a gas column capable of absorbing all the laser radiation. Consequently, a high temperature and pressure gas bubble (plasma phase) is formed inside the kerf, Fig. 12b. The plasma bubble has two main effects: it exchanges heat with the kerf walls and, together with the assist gas, pushes the molten basalt both out and towards the back of the kerf itself (as visible in Fig. 9 and Fig. 10). Downstream of the plasma bubble, the molten basalt flowing into the kerf continues to exchange heat with the kerf walls producing the resolidified material layer (the first layer described above) and further carbonisation, combustion, and vaporization of the matrix, Fig. 12c. This generates the second layer (consisting of matrix-free fibres), the debris formation (basalt droplets, carbonised matrix fragments), and further kerf and HAZ enlargement. The process is not stable, since the molten basalt must reach a certain volume before flowing into the kerf, this explains the presence of striations. The molten basalt flow inside the kerf, its partial expulsion, and cooling on the edge of the kerf are the cause of both the presence of the burr on both surfaces (the re-solidified basalt drops) and the characteristic wavy appearance of the kerf's edges, as visible in Fig. 7 and Fig. 8. The latter is confirmed by the analysis of the final part of the cut, Fig. 13, where it can be clearly seen that, on the upper surface of the kerf, the last part of the profile is very regular, while the more distant part is more irregular and damaged.

To have further confirmation of the interaction mechanisms, a new test was performed adopting the following process conditions: Pa = 4.5 kW, D = 0.15 ms, Ss = 2100 mm/s. During the test, cameras both in IR and visible spectra were adopted to record the interaction phenomena. The IR camera (FLIR mod A655SC) was selected since its spectral range (7.5–14 µm) is far enough from the laser beam wavelength to avoid the blinding phenomenon. During the test the following parameters were adopted: emissivity ε = 0.95, acquisition rate = 25 Hz, and a temperature range between 100 °C and 650 °C. It is worth noting that an emissivity ε in the range of 0.9–0.95 is a plausible value for the machined material. However, since it is not the correct value, this choice can affect the measurements. In the visible spectrum, a commercial camera was adopted (Canon FS100). In Fig. 14 and Fig. 15 four frames (at about 5 mm from the initial edge, at the middle of the sample, near the end of the cut, and immediately after the cut end) are reported for the IR and Visible camera, respectively.

From Fig. 14, during the cutting operation, the inner part of the kerf is at a temperature higher than the saturation one of the IR camera (600 °C). Moreover, as visible in Fig. 14d, immediately after the cut end, there is a large part of the kerf that is still at high temperature; this part is characterised by different striation, due to the molten basalt flow. While, in Fig. 15, it can be observed both the formation of a large plasma plume (in the opposite direction to the cutting one) and the droplets made of molten basalt (the red dots indicate by the arrow in Fig. 15d) that are still at high temperatures (since the red colours) and placed either inside or in the lower part of the kerf.

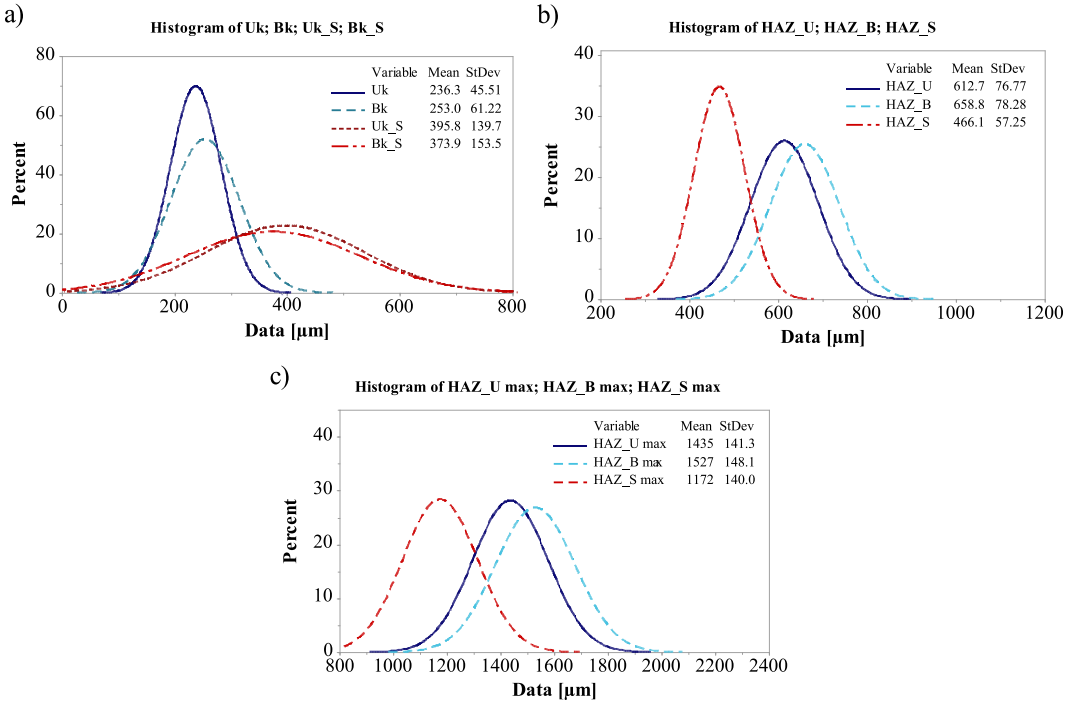

Fig. 19. Comparison between the distribution of the kerf width and HAZ extension: a) Kerf widths; b) HAZs; c) Maximum HAZs.

3.3. ANOVA results and effect of the process parameters

In Table 9 and Table 10, the ANOVA tables for the parameters measured in the section and on the surface are reported, respectively. In the table, the significant control factors (p-value < 0.05) are indicated by bold text. From the table, the cutting speed is the main significant control factor, since it affects all the response variables, except the HAZ_U that results unaffected by any process parameters. The pulse power affects the HAZ_B and the HAZ_B max. Conversely, the pulse duration seems does not affect any response variables. Moreover, no significant interactions are present. In any case, it is worth noting that the R-Sq [%] values do not appear exciting, since they are in the range of 30%-60%. This means that only 30%-60% of the response variables' variation is explained by the control factors. It is plausible that these low values are a consequence of the fact that, in addition to the laser action, both the kerf dimensions and the HAZ extension are influenced by the interaction between the kerf wall and the molten basalt flow generated downstream to the laser action. In Fig. 16–18, the main effect plots are reported for the section, upper kerf, and bottom kerf measurements, respectively. In the figures, the significant response variables are highlighted by a continuous line and full dots. As expected, since an increase in the cutting speed involves a decrease of the energy released for unit length (see Le in Table 5), the S increase involves kerf widths and HAZ extension reduction. About the effect of the pulse power on HAZ_B and HAZ_B max, the increase of Pp involves a decrease of both these quantities, this effect is opposite to then observed in CFRP laser cutting [60]. It is reasonable to assume that this effect is mainly due to how the molten basalt is formed and how the latter interacts with the surface of the kerf. As a matter of fact, the use of a high Pp implies a more violent interaction with the production of larger plasma bubbles at higher pressure, the latter favours the expulsion of the molten material out of the kerf reducing the HAZ enlargement.

4. Effect of measurement position

Previous studies show that the measurement position (section or surfaces) of the kerf characteristics (width and HAZ) influences the measurement itself [60,61,66,67]. Since, in laser cutting of BFRP, the kerf formation mechanism is quite different from that of CFRP, this aspect has deepened in the present section. Therefore, to investigate the effect of the measurement position a regression analysis was first performed between the average of the measurements carried out in the section and the ones acquired on the surfaces. During the analysis, a linear equation was adopted (however, the results remain similar even using other types of equations) and the p-value was assumed to verify the presence of correlation between the measured quantities (it means that a p-value < 0.05 indicates the presence of a significant correlation) while the R-Sq [%] parameter was adopted to measure how much the equation fit the data. The result of the analysis is summarised in Table 11. From the table, only the kerf widths are correlated to each other; while the HAZs show a p-value > 0.05. Then, no correlations are present between the HAZs. In any case, also for the kerf widths the correlation appears poor since the low values of R-Sq [%] due to the high data scattering. The latter is, probably, a consequence of the fact that the measuring positions between the sections and the surfaces are different. The analysis highlights that the damage mechanism on the external surfaces differs from that inside the kerf. Conversely, a correlation between the measurements of the kerf width is identified instead (albeit disturbed by noise).

In Fig. 19 the comparison between the distributions of the kerf widths and HAZs carried out in the different positions is reported. From the figure, the kerf widths measured in the section show mean values and standard deviations larger than the ones measured on the external surfaces. Therefore, the kerf measurements on the surface underestimate the quantities and vice versa. Conversely, the mean value of the HAZ extension measured on the external surfaces is larger than the ones measured in the section, while the standard deviation is almost equal. In addition, the measurements (width and HAZ extension) acquired on upper surfaces are slightly smaller than those obtained on the bottom surfaces. The differences observed between the widths measured on the surface and the one in the section are due to different phenomena, such as the erosion of the walls produced by the molten basalt flow inside the kerf, the possibility that part of the first layer may detach from the walls during the process or the sample manipulation. In addition, the typical

wavy shape of the kerf edge doesn't help since it may introduce an error in the width assessment. The differences found on the HAZ are always due to the flow of molten basalt which, on the external surfaces, forms several drops that flow and condense on the external surfaces. During its flow, the molten basalt exchanges heat with the matrix coating producing the matrix recession or its degradation (browning). This explains why the HAZ on the outside appears greater than that on the inside. Moreover, the difference between the upper and bottom surface characteristics, together with the observations about Fig. 13, indicate that, in the first part of the cut formation (i.e. in the area where the laser beam irradiates), the assist gas is still able to counteract the plasma bubble pressure. The differences observed in terms of kerf widths and HAZ extension pose a problem in the kerf estimation since, for a full characterisation of process and product, it is mandatory to measure both the positions (external and section). This aspect is often overlooked by academics.

5. Conclusion

In the present paper, laser cutting of BFRP laminate using a 450 W, QCW fiber laser is presented. Tests were carried out in the PW regime, to find the influence of the pulse power and duration on the maximum cutting speed. Then cutting tests were performed changing the pulse power, the pulse duration, and the cutting speed. The kerf geometry and quality were measured in the section and on the external surfaces. ANOVA analysis was adopted to assess the influence of the process parameters. From the results, within the adopted source, material, and process conditions, the main conclusions are:

- Basalt fibre composites can be easily cut by adopting a 450/4500 W QCW fibre laser working at a wavelength of $\lambda = 1070$ nm, at a cutting speed of up to 3500 mm/min.
- The maximum cutting speed depends on both the pulse power and the pulse duration; it increases as the pulse power increases and vice versa for the duration.
- From the cutting tests, the thermal damage mainly consists of matrix degradation, fibre protrusion, the presence of resolidified basalt droplets at the kerf edges and a layer of resolidified basalt mixed with carbonised matrix on the kerf wall.
- During the laser material interaction, plasma plume and molten basalt are produced. The pressure generated by the plasma, in combination with the pressure of the assist gas, pushes the molten basalt downstream to the laser beam inside the kerf, allowing further heat transfer on the kerf walls. During the heat transfer, an enlargement of both kerf and HAZ is produced.
- The kerf dimension and the HAZ extension are mainly affected by the cutting speed since this determines the energy released per unit of length and then, the overall interaction mechanism.
- Pulse power and pulse duration, although affect the maximum cutting speed, show a secondary effect on the kerf characteristics. Probably hidden by the effects of the molten basalt flow inside the kerf. The latter plays an important role in the interaction mechanisms and kerf formation.
- The regression tests show that only the widths are correlated between them. While the HAZs extensions are not correlated.
- In any case, the measuring position affects the measurement itself. The kerf widths measured in the section are larger than the ones measured on the external surfaces. Vice versa the HAZs extension. These differences are mainly due to the presence of molten basalt flow inside the kerf, too.

CRediT authorship contribution statement

C. Leone: Conceptualization, Methodology, Investigation, Data curation, Formal analysis, Resources, Writing – original draft, Writing – review & editing.. **R. Porcaro:** Methodology, Investigation, Data curation, Formal analysis, Writing – Original draft. **G. Campana:** Investigation, Formal analysis, Writing – Original draft.. **S. Genna:** Methodology, Investigation, Formal analysis, Writing – Original draft, Writing – review & editing.

Declaration of Competing Interest

The authors declare the following financial interests/personal relationships which may be considered as potential competing interests: Claudio Leone reports equipment, drugs, or supplies was provided by CIRTIBS Research Centre.

Data availability

Data will be made available on request.

Acknowledgements

The authors are particularly grateful to the Interuniversity Research Centre CIRTIBS of the University of Campania Luigi Vanvitelli, for providing part of the equipment to develop this research work.

References

[1] Morova N. Investigation of usability of basalt fibers in hot mix asphalt concrete. Constr Build Mater 2013;47:175–80. https://doi.org/10.1016/J.CONBUILDMAT.2013.04.048.
[2] Thorhallsson ER, Snaebjornsson JT. Basalt fibers as new material for reinforcement and confinement of concrete. Solid State Phenom 2016;249:79–84. https://doi.org/10.4028/WWW.SCIENTIFIC.NET/SSP.249.79.
[3] Monaldo E, Nerilli F, Vairo G. Basalt-based fiber-reinforced materials and structural applications in civil engineering. Compos Struct 2019;214:246–63. https://doi.org/10.1016/j.compstruct.2019.02.002.
[4] High C, Seliem HM, El-Safty A, Rizkalla SH. Use of basalt fibers for concrete structures. Constr Build Mater 2015;96:37–46. https://doi.org/10.1016/j.conbuildmat.2015.07.138.
[5] Saha S. A short review on the utilization of basalt fibres in concrete. RILEM Bookseries 2022;36:590–7. https://doi.org/10.1007/978-3-030-83719-8_51.
[6] Wang X, Wu Z, Wu G, Zhu H, Zen F. Enhancement of basalt FRP by hybridization for long-span cable-stayed bridge. Compos Part B Eng 2013;44:184–92. https://doi.org/10.1016/J.COMPOSITESB.2012.06.001.
[7] Bandaru AK, Ahmad S, Bhatnagar N. Ballistic performance of hybrid thermoplastic composite armors reinforced with Kevlar and basalt fabrics. Compos Part A Appl Sci Manuf 2017;97:151–65. https://doi.org/10.1016/j.compositesa.2016.12.007.
[8] Basalt Fiber n.d. https://www.basaltfiber-cn.com/products/basalt-fiber-cloth-basalt-fiber-fabric-weave (accessed June 15, 2022).
[9] Basalt fiber application|Basfiber n.d. https://basfiber.com/application (accessed September 12, 2022).
[10] Singha K. A short review on basalt fiber. Int J Text Sci 2012;2012:19–28. https://doi.org/10.5923/j.textile.20120104.02.
[11] Dhand V, Mittal G, Rhee KY, Park SJ, Hui D. A short review on basalt fiber reinforced polymer composites. Compos Part B Eng 2015;73:166–80. https://doi.org/10.1016/j.compositesb.2014.12.011.
[12] Fiore V, Scalici T, Di Bella G, Valenza A. A review on basalt fibre and its composites. Compos Part B Eng 2015;74:74–94. https://doi.org/10.1016/j.compositesb.2014.12.034.
[13] Lopresto V, Leone C, De Iorio I. Mechanical characterisation of basalt fibre reinforced plastic. Compos Part B Eng 2011;42:717–23. https://doi.org/10.1016/j.compositesb.2011.01.030.
[14] Bauer F, Kempf M, Weiland F, Middendorf P. Structure-property relationships of basalt fibers for high performance applications. Compos Part B Eng 2018;145:121–8. https://doi.org/10.1016/j.compositesb.2018.03.028.
[15] Scalici T, Pitarresi G, Badagliacco D, Fiore V, Valenza A. Mechanical properties of basalt fiber reinforced composites manufactured with different vacuum assisted impregnation techniques. Compos Part B Eng 2016;104:35–43. https://doi.org/10.1016/j.compositesb.2016.08.021.
[16] Carmisciano S, De RIM, Sarasini F, Tamburrano A, Valente M. Basalt woven fiber reinforced vinylester composites: Flexural and electrical properties. Mater Des 2011;32:337–42. https://doi.org/10.1016/J.MATDES.2010.06.042.
[17] Zhang H, Yao Y, Zhu D, Mobasher B, Huang L. Tensile mechanical properties of basalt fiber reinforced polymer composite under varying strain rates and temperatures. Polym Test 2016;51:29–39. https://doi.org/10.1016/J.POLYMERTESTING.2016.02.006.
[18] Lu Z, Xian G, Li H. Effects of elevated temperatures on the mechanical properties of basalt fibers and BFRP plates. Constr Build Mater 2016;127:1029–36. https://doi.org/10.1016/J.CONBUILDMAT.2015.10.207.

[19] Benmokrane B, Hassan M, Robert M, Vijay PV, Manalo A. Effect of Different Constituent Fiber, Resin, and Sizing Combinations on Alkaline Resistance of Basalt, Carbon, and Glass FRP Bars. J Compos Constr 2020;24:1–18. https://doi.org/10.1061/(asce)cc.1943-5614.0001009.

[20] Novitskii AG. High-temperature heat-insulating materials based on fibers from basalt-type rock materials. Refract Ind Ceram 2004.144–6.;2004(452):45. https://doi.org/10.1023/B:REFR.0000029624.43008.EF.

[21] Drozdyuk T, Aizenshtadt A, Tutygin A, Frolova M. Basalt fiber insulating material with a mineral binding agent for industrial use. IOP Conf Ser Mater Sci Eng 2016;124:012123. https://doi.org/10.1088/1757-899X/124/1/012123.

[22] Kim H. Enhancement of thermal and physical properties of epoxy composite reinforced with basalt fiber. Fibers Polym 2013.1311–6.;2013(148):14. https://doi.org/10.1007/S12221-013-1311-0.

[23] Sarasini F, Tirillò J, Sergi C, Seghini MC, Cozzarini L, Graupner N. Effect of basalt fibre hybridisation and sizing removal on mechanical and thermal properties of hemp fibre reinforced HDPE composites. Compos Struct 2018;188:394–406. https://doi.org/10.1016/j.compstruct.2018.01.046.

[24] Raponi E, Boria S, Giammaria V, Fischer B, Pörnbacher J, Sarasini F, et al. Effect of basalt intraply hybridization on the damage tolerance of flax laminates: Experimental analysis and analytical modeling under low-velocity impact. Compos Struct 2022;287:115270. https://doi.org/10.1016/j.compstruct.2022.115270.

[25] Prasad S, Chouhan H, Kartikeya K, Singh KK, Bhatnagar N. An experimental investigation into mechanical behaviour of Basalt PEI laminates at various strain rates. Compos Struct 2021;267:113800. https://doi.org/10.1016/j.compstruct.2021.113800.

[26] Russo P, Simeoli G, Cimino F, Papa I, Ricciardi MR, Lopresto V. Impact damage behavior of vinyl ester-, epoxy-, and nylon 6-based basalt fiber composites. J Mater Eng Perform 2019;28:3256–66. https://doi.org/10.1007/S11665-019-04037-8.

[27] Ricciardi MR, Papa I, Coppola G, Lopresto V, Sansone L, Antonucci V, et al. Effect of plasma treatment on the impact behavior of epoxy/basalt fiber-reinforced composites: a preliminary study. Polymers (Basel) 2021;13:1293. https://doi.org/10.3390/polym13081293.

[28] Lee SO, Rhee KY, Park SJ. Influence of chemical surface treatment of basalt fibers on interlaminar shear strength and fracture toughness of epoxy-based composites. J Ind Eng Chem 2015;32:153–6. https://doi.org/10.1016/J.JIEC.2015.08.009.

[29] Bhat T, Chevali V, Liu X, Feih S, Mouritz AP. Fire structural resistance of basalt fibre composite. Compos Part A Appl Sci Manuf 2015;71:107–15. https://doi.org/10.1016/j.compositesa.2015.01.006.

[30] Micelli F, Aiello MA. Residual tensile strength of dry and impregnated reinforcement fibres after exposure to alkaline environments. Compos Part B Eng 2019;159:490–501. https://doi.org/10.1016/j.compositesb.2017.03.005.

[31] Lu Z, Xian G. Resistance of basalt fibers to elevated temperatures and water or alkaline solution immersion. Polym Compos 2018;39:2385–93. https://doi.org/10.1002/PC.24220.

[32] Elgabbas F, Ahmed EA, Benmokrane B. Physical and mechanical characteristics of new basalt-FRP bars for reinforcing concrete structures. Constr Build Mater 2015;95:623–35. https://doi.org/10.1016/J.CONBUILDMAT.2015.07.036.

[33] Abrate S, Walton DA. Machining of composite materials. Part I: Traditional methods Compos Manuf 1992;3:75–83. https://doi.org/10.1016/0956-7143(92)90119-F.

[34] Teti R. Machining of composite materials. CIRP Ann - Manuf Technol 2002;51:611–34. https://doi.org/10.1016/S0007-8506(07)61703-X.

[35] Ramulu M. Machining and surface integrity of fibre-reinforced plastic composites. Sadhana 1997;22:449–72. https://doi.org/10.1007/BF02744483.

[36] Abrate S, Walton D. Machining of composite materials. Part II: Non-traditional methods Compos Manuf 1992;3:85–94. https://doi.org/10.1016/0956-7143(92)90120-J.

[37] Shanmugam DK, Nguyen T, Wang J. A study of delamination on graphite/epoxy composites in abrasive waterjet machining. Compos Part A Appl Sci Manuf 2008;39:923–9. https://doi.org/10.1016/j.compositesa.2008.04.001.

[38] Shanmugam DK, Chen FL, Siores E, Brandt M. Comparative study of jetting machining technologies over laser machining technology for cutting composite materials. Compos Struct 2002;57:289–96. https://doi.org/10.1016/S0263-8223(02)00096-X.

[39] Ramraji K, Rajkumar K, Dhananchezian M, Sabarinathan P. Key Experimental Investigations of cutting dimensionality by Abrasive Water Jet Machining on Basalt Fiber/Fly ash Reinforced Polymer Composite. Mater Today Proc 2019;22:1351–9. https://doi.org/10.1016/j.matpr.2020.01.428.

[40] Ramraji K, Rajkumar K, Rajesh M, Gnanavelbabu A. A Comparative Study on Abrasive Water Jet Machining Characteristics of Entry and Exit Layers of Glass and Basalt Woven Polymer Composites. Springer Singapore 2021. https://doi.org/10.1007/978-981-15-4745-4_4.

[41] Amuthakkannan P, Manikandan V, Uthayakumar M, ArunPrasath K, Sureshkumar S. Investigation of the machining performance of basalt fiber composites by abrasive water jet machining. Mater Phys Mech 2021;47:830–42. https://doi.org/10.18149/MPM.4762021_3.

[42] Sathishkumar N, Selvam R, Kumar KM, Abishini AH, Rahman TK, Mohanaranga S. Influence of garnet abrasive in drilling of Basalt–Kevlar–Glass fiber reinforced polymer cross ply laminate by Abrasive Water Jet Machining process. Mater Today Proc 2022. https://doi.org/10.1016/j.matpr.2022.04.861.

[43] Leone C, Genna S, Caggiano A, Tagliaferri V, Molitierno R. Influence of process parameters on kerf geometry and surface roughness in Nd:YAG laser cutting of Al 6061T6 alloy sheet. Int J Adv Manuf Technol 2016;87:2745–62. https://doi.org/10.1007/s00170-016-8667-4.

[44] Leone C, Genna S, Tagliaferri V. Cutting of AA6061 by a multimode pulsed Nd:YAG laser with high pressure gas: characterisation of kerf geometry and quality. Int J Adv Manuf Technol 2018;94:925–40. https://doi.org/10.1007/s00170-017-0804-1.

[45] Karatas C, Keles O, Uslan I, Usta Y. Laser cutting of steel sheets: Influence of workpiece thickness and beam waist position on kerf size and stria formation. J Mater Process Technol 2006;172:22–9. https://doi.org/10.1016/j.jmatprotec.2005.08.017.

[46] Fomin VM, Golyshev AA, Malikov AG, Orishich AM, Shulyat'ev VB.. Mechanical characteristics of high-quality laser cutting of steel by fiber and CO2 lasers. J Appl Mech Tech Phys 2015;56:726–35. https://doi.org/10.1134/S0021894415040203.

[47] Genna S, Menna E, Rubino G, Tagliaferri V. Experimental investigation of industrial laser cutting: The effect of the material selection and the process parameters on the kerf quality. Appl Sci 2020;10:4956. https://doi.org/10.3390/app10144956.

[48] Tönshoff HK, Emmelmann C. Laser cutting of advanced ceramics. CIRP Ann - Manuf Technol 1989;38:219–22. https://doi.org/10.1016/S0007-8506(07)62689-4.

[49] Cenna AA, Mathew P. Analysis and prediction of laser cutting parameters of fibre reinforced plastics (FRP) composite materials. Int J Mach Tools Manuf 2002;42:105–13. https://doi.org/10.1016/S0890-6955(01)00090-6.

[50] Goeke A, Emmelmann C. Influence of laser cutting parameters on CFRP part quality. Phys. Procedia, vol. 5, Elsevier B.V.; 2010, p. 253–8. https://doi.org/10.1016/j.phpro.2010.08.051.

[51] Mathew J, Goswami GL, Ramakrishnan N, Naik NK. Parametric studies on pulsed Nd:YAG laser cutting of carbon fibre reinforced plastic composites. J Mater Process Technol 1999;89–90:198–203. https://doi.org/10.1016/S0924-0136(99)00011-4.

[52] Chryssolouris G. Laser Machining: Theory and Practice,. New York,: 1991.

[53] Gautam GD, Mishra DR. Dimensional accuracy improvement by parametric optimization in pulsed Nd:YAG laser cutting of Kevlar-29/basalt fiber-reinforced hybrid composites. J Brazilian Soc Mech Sci Eng 2019;41:1–22. https://doi.org/10.1007/S40430-019-1783-Y.

[54] Gautam GD, Mishra DR. Parametric investigation in pulsed Nd:YAG laser cutting of Kevlar-Basalt fiber composite. Lasers Manuf Mater Process 2020;7:373–98. https://doi.org/10.1007/S40516-020-00125-Z.

[55] Gautam GD, Mishra DR. Firefly algorithm based optimization of kerf quality characteristics in pulsed Nd:YAG laser cutting of basalt fiber reinforced composite. Compos Part B Eng 2019;176:107340. https://doi.org/10.1016/j.compositesb.2019.107340.

[56] Jain A, Agarwal A, Chauhan PS. Optimization of laser cutting quality characteristics for basalt –glass hybrid composite using hybrid approach. Mater Today Proc 2022;62:6578–82. https://doi.org/10.1016/j.matpr.2022.04.578.

[57] Najjar IMR, Sadoun AM, Abd Elaziz M, Abdallah AW, Fathy A, Elsheikh AH. Predicting kerf quality characteristics in laser cutting of basalt fibers reinforced polymer composites using neural network and chimp optimization. Alexandria Eng J 2022;61:11005–18. https://doi.org/10.1016/j.aej.2022.04.032.

[58] Mendes M, Sarrafi R, Schoenly J, Vangemert R. Fiber laser micromachining in high-volume manufacturing. accessed September 16, 2022 Laser Focus World 2015. https://www.laserfocusworld.com/industrial-laser-solutions/article/14216389/fiber-laser-micromachining-in-highvolume-manufacturinganufacturing.pdf.

[59] Maybe the most flexible laser—ever! Laser Focus World 2015. https://www.laserfocusworld.com/industrial-laser-solutions/article/14216362/maybe-the-most-flexible-laserever (accessed September 16, 2022).

[60] Leone C, Mingione E, Genna S. Laser cutting of CFRP by Quasi-Continuous Wave (QCW) fibre laser: Effect of process parameters and analysis of the HAZ index. Compos Part B Eng 2021;224:109146. https://doi.org/10.1016/J.COMPOSITESB.2021.109146.

[61] Leone C, Mingione E, Genna S. Interaction mechanisms and damage formation in laser cutting of CFRP laminates obtained by recycled carbon fibre. Int J Adv Manuf Technol 2022;121:407–27. https://doi.org/10.1007/S00170-022-09313-X.

[62] Basalt fabrics at low price n.d. https://basfiber.com/products/fabrics (accessed June 15, 2022).

[63] Mates. SX8EVO data sheet n.d. https://fileserver.mates.it/Prodotti/2_Matrici/TDS/Resine/Mates/SX8_EVO_DS.pdf (accessed June 15, 2022).

[64] Qin T, Zhong Z, Jiao H, Zhou L, Huang Y, Long Y. Experimental study on gas-assisted laser cutting carbon fiber reinforced plastics. Int J Adv Manuf Technol 2022;119:6361–70. https://doi.org/10.1007/S00170-021-08467-4/FIGURES/14.

[65] Leone C, Pagano N, Lopresto V, De Iorio I. Solid state Nd:YAG laser cutting of CFRP sheet: Influence of process parameters on kerf geometry and HAZ. ICCM Int Conf Compos Mater 2009:1–10. http://iccm-central.org/Proceedings/ICCM17pr.

[66] Tagliaferri V, Visconti Crivelli I. Machining of fibre reinforced materials with laser beam: cut quality evaluation. Proc. Eur. Conf. Compos. Mater., London, Uk: Elsevier; 1987, p. 190–9.

[67] Jovane F, Di Ilio A, Tagliaferri V, Veniali F. Laser Machining of Composite Materials. In: Martellucci S, Chester AN, Scheggi AM, editors. Laser Appl. Mech. Ind. NATO ASI S, Dordrecht, The Netherlands: Springer; 1993, p. 115–29. https://doi.org/10.1007/978-94-011-1990-0_7.

[68] Leone C, Genna S, Tagliaferri V. Fibre laser cutting of CFRP thin sheets by multi-passes scan technique. Opt Lasers Eng 2014;53:43–50. https://doi.org/10.1016/j.optlaseng.2013.07.027.

[69] Li M, Li S, Yang X, Zhang Y, Liang Z. Fiber laser cutting of CFRP laminates with single- and multi-pass strategy: A feasibility study. Opt Laser Technol 2018;107:443–53. https://doi.org/10.1016/j.optlastec.2018.06.025.

[70] Li M, Li S, Yang X, Zhang Y, Liang Z. Effect of lay-up configuration and processing parameters on surface quality during fiber laser cutting of CFRP laminates. Int J Adv Manuf Technol 2019;100:623–35. https://doi.org/10.1007/s00170-018-2728-9.

[71] Rao S, Sethi A, Das AK, Mandal N, Kiran P, Ghosh R, et al. Fiber laser cutting of CFRP composites and process optimization through response surface methodology. Mater Manuf Process 2017;32:1612–21. https://doi.org/10.1080/10426914.2017.1279296.

[72] Montgomery DC. Design and Analysis of Experiments. 10th ed. New York, NY: Wiley; 2019.

[73] Coleman DE, Montgomery DC. A systematic approach to planning for a designed industrial experiment. Technometrics 1993;53:1–12. https://doi.org/10.1080/00401706.1993.10484984.